Estimation and Assessment of Errors Related to Antenna Pattern Distortion in CODAR SeaSonde High-Frequency Radar Ocean Current Measurements

KENNETH LAWS

University of California, Santa Cruz, Santa Cruz, California

JEFFREY D. PADUAN

Naval Postgraduate School, Monterey, California

JOHN VESECKY

University of California, Santa Cruz, Santa Cruz, California

(Manuscript received 22 July 2008, in final form 28 October 2009)

ABSTRACT

A simulation-based investigation of errors in HF radar–derived, near-surface ocean current measurements is presented. The simulation model is specific to Coastal Ocean Dynamics Application Radar (CODAR) SeaSonde radar systems that employ a compact, collocated antenna geometry. In this study, radial current retrievals are obtained by processing simulated data using unmodified CODAR data processing software. To avoid limiting the results to specific ocean current and wind wave scenarios, the analyses employ large ensembles of randomly varying simulated environmental conditions. The effect of antenna pattern distortion on the accuracy of retrievals is investigated using 40 different antenna sensitivity patterns of varying levels of distortion. A single parameter is derived to describe the level of the antenna pattern distortion. This parameter is found to be highly correlated with the rms error of the simulated radial currents ($r = 0.94$) and therefore can be used as a basis for evaluating the severity of site-specific antenna pattern distortions. Ensemble averages of the subperiod simulated current retrieval standard deviations are found to be highly correlated with the antenna pattern distortion parameter ($r = 0.92$). Simulations without distortions of the antenna pattern indicate that an rms radial current error of 2.9 cm s^{-1} is a minimum bound on the error of a SeaSonde ocean radar system, given a typical set of operating parameters and a generalized ensemble of ocean conditions.

1. Introduction

With the large-scale deployment of high-frequency (HF) radar systems for mapping near-shore ocean surface currents as a part of large-scale coastal environmental monitoring projects (e.g., Paduan et al. 2004), ocean radar systems are transitioning from an experimental to an operational oceanographic tool. Increasingly, datasets are being collected over longer periods of time and larger areas of the world's coastal oceans. In the United States, data products are now being delivered to national networks and made available to the public and to the research community in near–real time (e.g., see online at http://www.cencoos.org/currents). As the scope of ongoing HF radar current monitoring projects increases, the benefits of assimilating of HF radar–obtained current fields into ocean circulation models increases correspondingly (see, e.g., Breivik and Saetra 2001; Paduan and Shulman 2004; Shulman and Paduan 2008). Presently, a leading factor limiting this assimilation is insufficient knowledge of uncertainties in the radar data.

HF radar vector current measurements are obtained from radial component current measurements that go into a vector summation. Therefore, it is first at the radial level where the errors need to be understood. Other potential sources of errors in vector currents, such as subgrid horizontal shear and distribution of HF radar sampling cells, also exist but are not considered here. Errors in the radials result from several known factors,

Corresponding author address: Kenneth Laws, Baskin School of Engineering, University of California, Santa Cruz, 1156 High St., Santa Cruz, CA 95064.
E-mail: kip@soe.ucsc.edu

DOI: 10.1175/2009JTECHO658.1

such as limitations resulting from noise and interference in the received signals; distortions in the radar antenna sensitivity patterns; inherent limitations in signal processing methods; and limitations in the frequency resolution of the Doppler spectrum, which translates directly to current magnitude resolution. Some recent studies that have investigated errors in radial current estimates based on experiments using in situ or radar-to-radar comparisons include Emery et al. (2004), Lipa et al. (2006), and Paduan et al. (2006).

Errors in the radial current estimates are dependent on the signal processing methods used to resolve the angular position of a given current estimate. A detailed discussion of the two most prominent methods is given by Barrick and Lipa (1997). The first and more easily understood of these two methods is beam forming. In this approach, the radar's receive antenna consists of a distributed array of elements that is electronically steered to form a narrow sensitivity beam, using the delay and sum technique (see, e.g., Milligan 2005). The width of the formed beam determines the angular resolution and is dependent on the length of the array and the transmit frequency. The width and pointing angle of the steered beam and the range resolution determine the size and location of the radar resolution cell (the area of ocean surface corresponding to the surface current measurement). The current estimate is then derived from the Doppler spectrum by finding the centroids of the Doppler shifted Bragg peaks. Less straightforward is the direction finding approach where each Doppler velocity in a broad angle spectrum is processed to determine the direction or directions of arrival of the received ocean echo signal. The primary advantage of the second approach is the elimination of the need for long receive antenna arrays. Direction finding can be done with compact, collocated loop and monopole antennas requiring little more coastal footprint than a vertical pole supporting both receive and transmit antennas. Most commonly used algorithms for direction finding with ocean radar systems are based on the Multiple Signal Characterization (MUSIC) algorithm developed by Schmidt (1982, 1986) and applied to ocean radar systems (Barrick and Lipa 1997).

The MUSIC algorithm has the ability to resolve multiple directions of arrival for a given spectral component (radial current magnitude) of the radar Doppler spectrum. The maximum number of directions that can be uniquely determined for a given velocity is equal to the lesser of either one less than the number of antennas in the receive array or the number of individual (assumed independent) spectra that are collected for a given inversion. If the number of independent spectra is large, a high degree of certainty is obtained in determining the number of directions for a given Doppler shift (and hence a given radial current magnitude). Unfortunately, because of the frequency and sampling time limitations of practical ocean radar systems, the number of spectra is not large [in the case of typical Coastal Ocean Dynamics Application Radar (CODAR) operating parameters, three spectra are used]; hence, the determination of the number of directions is uncertain (for a detailed comparison of beam forming and direction finding, see Laws et al. 2000).

In installing new radar sites and maintaining existing installations, it is important, particularly with compact antenna configuration systems, to know the characteristics of the antenna sensitivity patterns and to calibrate the radar system accordingly using the data processing software. Effects of antenna pattern distortion on radial current maps, such as angular sectors with reduced numbers of current solutions or apparently nonphysical current solutions, have been observed and empirically associated with antenna pattern distortions. Studies have shown that measured patterns improve results (e.g., Kohut and Glenn 2003; Paduan et al. 2006), but it is likely that distorted patterns reduce the accuracy or coverage of radar systems and that these effects are only partially mitigated by use of pattern measurements.

Because of the difficulty and expense in obtaining comprehensive in situ data and the inherent differences between available in situ data and HF radar measurements, quantitative analyses relating observed radial current errors to antenna pattern distortions are impractical. The factors that affect the patterns are generally part of the radar site environment and not easily varied experimentally. Further, the performance of the radar is essentially statistical, and long time series are needed for substantive evaluations. For this reason, and the need for an independent measure of truth, we rely on simulation-based analysis in the work presented here.

2. Simulation strategy

In this simulation-based analysis, errors in radial current estimates and their relationship to the radar system are investigated with a specific focus on the effect of imperfect antenna patterns. Because most radar systems in use today are CODAR SeaSondes, these simulations are modeled on that system's configuration and made compatible with that system's data processing software.

Previous studies that employed simulation methods have investigated various factors determining errors, including signal-to-noise ratio (SNR), setting of radar parameters, effects of the current field under measurement, and antenna pattern distortions. D. E. Barrick and

B. J. Lipa (1996, personal communication) used simulations to compare performance of beam forming and MUSIC direction finding methods. They employed specific current scenarios including upwelling and current front, but they did not examine effects of SNR. Laws et al. (2000) used simulations with specific scenarios, including uniform current and a current jet, to compare MUSIC and beam forming methods. They also examined effects of overall SNR and a ''shading'' scenario where SNR was reduced over a fraction of the coverage area. Their results indicated a power law response in rms error with SNR for beam forming but a nearly flat response for MUSIC. Toh (2005) used simulation methods with specific current profiles to examine errors with SeaSonde radar systems. He obtained some results indicating that rms errors increase with the square root of the SNR, but other results were inconsistent. He also examined effects of distorted antenna patterns. De Paolo and Terrill (2007), in their simulation study, looked at several wind and current scenarios, including onshore and cross-shore winds and uniform, shear, and eddy current scenarios. They also looked at the effects of SNR, and their results demonstrate a flat response in MUSIC ''skill'' above about 11 dB. They did not include antenna distortions. In all of the above cases, SNR refers to the spectral region of the Bragg peak, not a particular spectral component within the peak.

The goals of the work presented here are to build on previous work in two key aspects: 1) to provide a more quantitative analysis of antenna pattern distortion effects than has been done previously and 2) to present results that are more general in nature and not dependent on a specific set of sea surface conditions. Central to these goals is the need to isolate particular parameters of interest by removing or generalizing the effects of other parameters on the radial current uncertainty. The characteristics of the current field present at the time of the measurement affect the uncertainty of a given measurement within the field (Laws et al. 2000). Therefore, a single simulation with a given current scenario produces a result that is specific to that scenario. Previous studies provide useful analyses by examining selected scenarios with specific desired characteristics, but the problem of how the radial current uncertainty depends on current field is difficult to quantify. Further, even if one could fully describe the dependence of radial current uncertainty on the current field, in practice, the current field is only known through the estimates obtained. Results that are more generally applicable to radar measurement uncertainties are desired and are obtained here through simulations that employ large ensembles of randomly generated current field scenarios with appropriate statistical characteristics.

For simplicity, we assume that the radar signal is only due to first-order backscatter originating from the simulated sea region within an annular ring centered on the radar system, with a width corresponding to the radar range resolution and a radius corresponding to the selected radar range bin. Hence, we can also assume that only the properties of the currents present in the range arc defined by the range bin and the sea region affect the accuracy of the retrievals. As mentioned above, the nature of variations in radial current magnitude has been observed to affect the accuracy of retrievals. We suggest that the properties of the radial current magnitude within a single range arc that affect the MUSIC retrievals include the rate of change of the radial current as a function of azimuth, variations in that rate of change, maximum and minimum current values, and the number of extrema. This last property relates to the occurrence of multiple azimuthal locations corresponding to a single radial current magnitude. For the purpose of this simulation, what matters is that the radial current profile over the range arc is sufficiently complicated to challenge the inversion algorithm and that it is realistic in nature. Simulated radial currents are generated using a large ensemble of random, physically plausible, current scenarios based on a variable shear scenario superimposed over a variable uniform current. These scenarios are defined over a rectangular simulation grid that contains the range arc region. The angular profiles over the range arc of the radial currents generated by these scenarios exhibit a wide variety of the desired properties listed above. Different physical scenarios, such as eddies and jets, would also produce radial current profiles with a variety of shears and extrema depending on the specific scenario. It is the objective of this work to derive results that are not dependent on a specific type of radial current profile but rather correspond to a random ensemble of current profiles that contain a wide variety of the pertinent parameters that challenge the MUSIC algorithm's current retrieval process, much the same as what would be observed in the real world.

3. Approach

a. Data description

For a SeaSonde radar system operating in the field, the raw data collected are time series of backscatter signals from a frequency modulated interrupted continuous wave (FMICW) transmitted signal. The first stage of the processing involves demodulating the received signal to separate signals coming from different ranges from the radar. Signals, thus separated, arise from areas of sea surface within annular rings centered

on the radar system of a radius r, depending on the selected range bin and effective width, $\Delta r \approx c/2b$, where b is the bandwidth of the transmitted radar signal and c is the speed of light. A fast Fourier transform (FFT) is applied to the range bin data to obtain Doppler spectra for the given range bin. It is commonly assumed that the range resolution processing is well understood and not a significant contributor to errors in the current retrievals. For simplicity, we begin with the simulation of signals that arise only from the range arc corresponding to the selected range bin.

The simulation is defined on a Cartesian grid, and the radar system is located at the center. A grid resolution of one-eighth the radar range resolution is used so that the effects of current variability over the radar resolution cell are included in the simulated radar data. The radar backscatter from simulated Bragg resonant ocean waves is computed for a limited range of angles, referred to as the sea arc, based on a simulated wave spectrum and ocean current. The radar echo for the remaining angular region is defined to be zero. For the simulations presented here, the range of the sea arc is either set to −30° to 180° or set by the angular region obtained from field site antenna pattern measurements. The selection of the sea arc region is somewhat arbitrary, but by limiting the sea arc to less than 360°, the simulated data reflects conditions that are commonly seen in the field (i.e., the presence of a limit or edge of the sea arc region). Signals from each of the simulation grid points within the range arc are summed to compute the total radar backscatter.

A radar frequency of 12 MHz and a bandwidth of 49 kHz are used giving a range resolution of about 3.0 km. The transform length and sampling frequency of the radar are 512 points and 2.0 Hz, respectively. These radar parameters were adopted from an operational CODAR system in the field at Monterey Bay. Range bin 7 is selected for these simulations along with an angular resolution of 5°, producing a radar resolution cell with 2 km by 3 km horizontal dimensions.

Simulated radar backscatter data are complex amplitude time series for each antenna element. Radar cross and self-spectra are given by

$$S_{j,k} = s_j s_k^*, \tag{1}$$

where s_j and s_k are the Doppler spectra collected on antenna elements j and k ($j = 1, 2, 3$; $k = 1, 2, 3$) and the asterisk indicates the complex conjugate. Antenna 3 is a monopole with isotropic ideal sensitivity pattern, and antennas 1 and 2 are crossed dipole antennas with sinusoidal ideal sensitivity patterns and sensitivity nulls oriented at 90° relative to each other. The simulated cross and self-spectra are computed and written to a CODAR-compatible spectra data file for processing for currents.

It is assumed that the sea echo is dominated by first-order Bragg scatter and that all other contributions, including higher-order backscatter, can be neglected. The simulated backscattered electromagnetic amplitude from the sea surface is given by

$$E = \gamma \exp(i\omega_r t)[A_+ \exp(-i\Delta\omega_- t) + A_- \exp(-i\Delta\omega_+ t)], \quad \text{with} \tag{2}$$

$$\Delta\omega_\pm = \omega_c \pm \omega_B, \tag{3}$$

where γ is a constant used to set the backscatter amplitude, ω_r is the radar transmit angular frequency, ω_B is the Doppler shift resulting from the still water phase velocity of the Bragg resonant waves, and ω_c is the Doppler shift resulting from the radial component of the current. The simulated spectra are effectively shifted to zero center frequency, and the radar frequency ω_B is not included in the simulated data. For the ocean surface, the complex amplitudes A_+ and A_- are best described by zero-mean Gaussian random variables with variance proportional to the spectral energy of the resonant waves (Barrick and Snider 1977). Therefore, the magnitudes of both the real and imaginary parts of the simulated complex amplitudes are independent and randomly distributed in space over the simulation grid. The amplitudes are assumed to be constant over the 4.3-min sampling time typical for CODAR standard range systems. The resonant waves are assumed to result from local wind, and the wind wave energy spectrum is that described by Pierson and Moskowitz (1964) for fully developed seas.

The variance of A_+ and A_- are set proportional to the simulated Bragg wave spectral energy. The backscatter amplitude is not critical, because it primarily affects the SNR of the resonant peaks, which is not the focus of these simulations. The scaling factor γ is set so that the Bragg peaks in the simulated spectra are roughly equal in amplitude to those observed experimentally with CODAR systems in the field. Directional spreading of the wind wave energy is accounted for by the modified cardioid function (Longuet-Higgins et al. 1963),

$$G(\theta_r, \theta_w) = \alpha + (1 - \alpha)\cos^4\left(\frac{\theta_r - \theta_w}{2}\right), \tag{4}$$

where $\alpha = 0.01$ accounts for resonant wave energy opposite the wind direction, θ_w is the wind direction (toward), and θ_r is the propagation direction of the Bragg resonant waves. The spectral energy of the Bragg resonant waves is then

$$W(\theta_r, \theta_w) = G(\theta_r, \theta_w)W_u, \quad (5)$$

where W_u is the spectral energy of the wind waves with wavelength equal to half the radar wavelength aligned with the wind direction, as derived from the simulated wind wave energy spectrum. This directional wave height dependence gives rise to a variation in the ratio of the signals resulting from the approaching and receding Bragg resonant waves. The simulated backscatter from the sea surface is computed assuming a uniform illumination of the sea surface. Effects of propagation loss are not included. The simulated antenna voltages were computed using either the ideal antenna pattern, measured antenna patterns from selected radar sites, or simulated distorted patterns.

The CODAR data processing algorithm requires multiple assumed independent spectra for a single inversion producing radial current estimates. Settings used to process the simulated data are typical for field systems in the California coastal region. The spectra sample size was 512 points, and the sampling rate was 0.5 s, giving a time per spectra of about 4.3 min. The averaging time for spectra was 15 min, but a 50% overlap between averaged spectra was allowed so that averaged spectra were produced at 10-min intervals. These spectra were inverted to produce maps of estimates of the radial currents over the given range arc. Seven maps were accumulated over each 74-min interval and merged, by taking the median value wherever there were multiple estimates of radials obtained for the same radar resolution cell, to produce the radial current output files. The overlap of the 74-min intervals was allowed so that output files were generated at hourly intervals.

The radials contained in the 10-min maps, referred to as subperiod radials, are generally not retained by the data processing software, but some statistics of the subperiod radials are computed and recorded with the hourly radial output files. In particular, for each radar resolution cell, the number of subperiod radials that are merged to produce the radial current estimate output and the standard deviation of those subperiod radials are recorded in the radial output files. This standard deviation is referred to by CODAR as the temporal quality and labeled ''tempQual'' in the radial output files. The method of merging the subperiod radials (either the mean or median function) to compute the hourly maps is user selectable in CODAR's software. The error in the simulated radial current estimates is defined as the difference between the retrieved radial current estimate for a given radar resolution cell and the average radial component of the simulated currents within that cell.

b. Simulating the sea surface state

In defining ocean wave and current scenarios, our desire is to create physically plausible situations that lead to a variety of sufficiently complicated radial current profiles. To reasonably challenge the data inversion algorithm, these situations include cases that contain two or more azimuthal locations for some of the radial currents in the given range arc. Sufficiently complicated current patterns are obtained by defining two independent currents over the simulation grid, summed to produce the total current. The first current is defined parallel to a simulated wind with a magnitude of 3% of the wind speed, based roughly on estimates of wind-driven surface currents (Wu 1975). The wave energy and hence the radar backscatter amplitudes are related to the wind as described in the previous section. Because the SNR of the simulated data was set high enough so as not to be a factor in this study, the only expected significant effect of the wind–wave spectrum on the simulated data is its effect on the amplitude of the signal arising from approaching Bragg waves relative to the signal arising from receding Bragg waves. The dependence of this simulated current component on wind speed was chosen to roughly preserve a correlation between Bragg peak energy and currents as expected in real conditions. The value of the proportionality constant was selected to be reasonable but not thought to be important. The direction of the current relative to the wind was also thought not to be important but in retrospect should have included a clockwise rotation resulting from the Coriolis force. The maximum wind speed possible was set to about 11 m s^{-1}, giving a maximum for this current component of about 33 cm s^{-1}. The minimum wind speed was set to about 2 m s^{-1}. The wind direction was uniformly distributed over all angles.

The second current component is independent of the wind and defined parallel to a given ''shear line'' that divides the simulation grid into two parts. A current speed is defined for each of these regions on the grid. A sine function is used to smoothly transition the current speed between the two regions. The minimum width of the shear region is limited to 10 km and the maximum current variation across the shear region is limited to 45 cm s^{-1}. The resulting maximum simulated current shear is 7.1×10^{-5} s^{-1}. This is comparable to the maximum observed shear (about 10^{-4} s^{-1}) observed in the inshore edge of the Gulf Stream (Sheres et al. 1985). Although the random current scenarios generate a wide variety of radial current profiles, the maximum currents simulated are limited to about 75 cm s^{-1}. Regions where very high current magnitudes are expected (e.g., the Florida Current, where speeds up to 2 m s^{-1} are

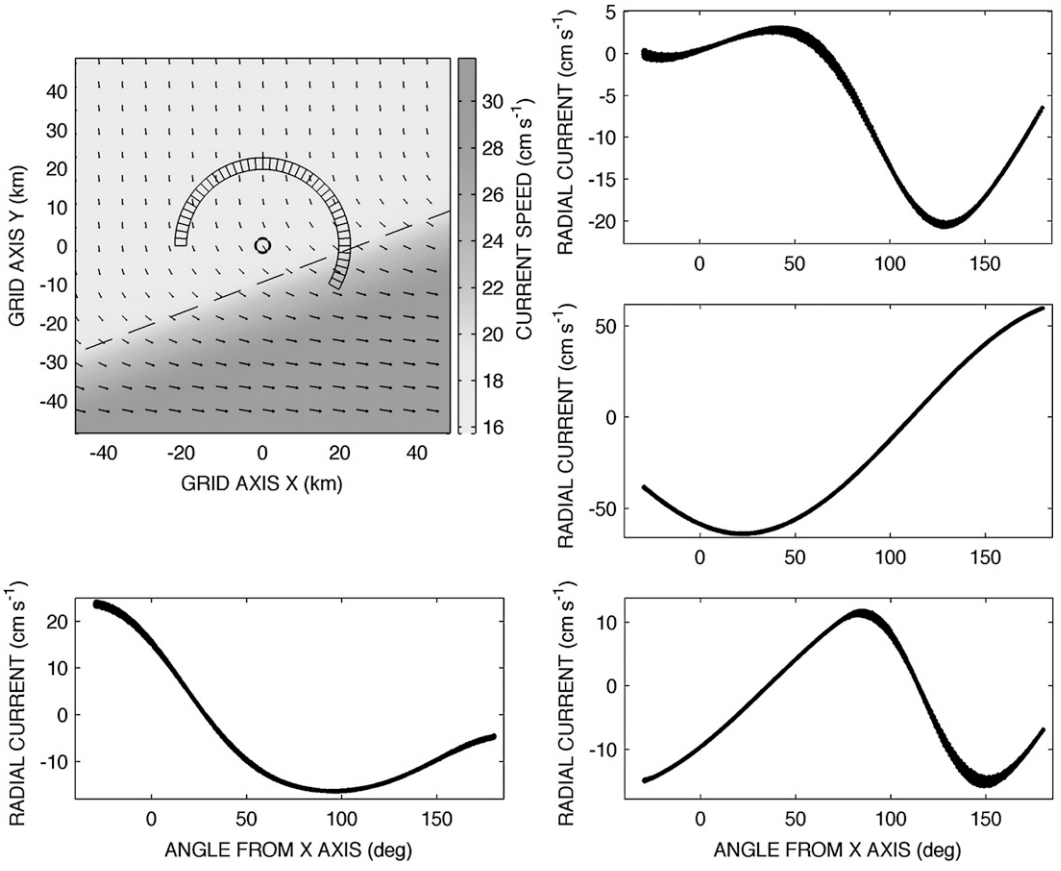

FIG. 1. (top left) Simulation geometry showing the radar system location (black circle at center) and the 5° resolution cells of a single range bin selected for generating the sea echo (concentric annular ring around the radar with divisions every 5°). The simulated current scenario shown is a sum of a uniform simulated wind-driven current and an additional current with a shear feature. The shear is perpendicular to the dashed line diagonally crossing the simulation grid. (bottom left) The corresponding radial current is shown. The width of the line indicates the radial current variation over the radar range resolution. (right) Selected examples of radial current profiles corresponding to randomly generated current scenarios are shown. (top) A profile with both a weak current region and a stronger current region with double angle solutions is shown. (middle) An example of stronger currents with a large current variation is shown. (bottom) A profile with current speeds that have double and triple angle solution regions is shown.

observed) are not accounted for within the work presented here and are left for future investigations.

This method of defining the current over the simulation grid requires seven parameters to fully describe the sea surface scenario. These parameters are wind speed, wind direction, slope and intercept of the current shear line, current magnitude for each of the two regions, and the width of the shear region. An example of a sea surface scenario generated in this manner and the corresponding radial current profile are shown in Fig. 1, along with selected examples showing some of the variation in characteristics of the random radial current profiles. The radial current profiles generated in this way provide a wide variety of situations that challenge the MUSIC algorithm, including variation in the rate of change in current speeds; single, double, and triple angle solution cases; weak current as well as strong current cases; and large variation in currents over the range arc. They do not contain very large currents, and they do not contain extremely sharp or discontinuous changes in current.

c. Generalization of sea surface state scenario

As discussed above, properties of the sea surface conditions that affect the retrieval of currents are limited to a single range arc. Properties of the radial currents within the arc that we consider important for this simulation study include maximum and minimum radial current, rate of change of radial current versus look angle, number of unique angular solutions for each current speed (quantized by the radar's current speed and angular resolution), and directional energy of the Bragg resonant waves (related to the wind direction, as

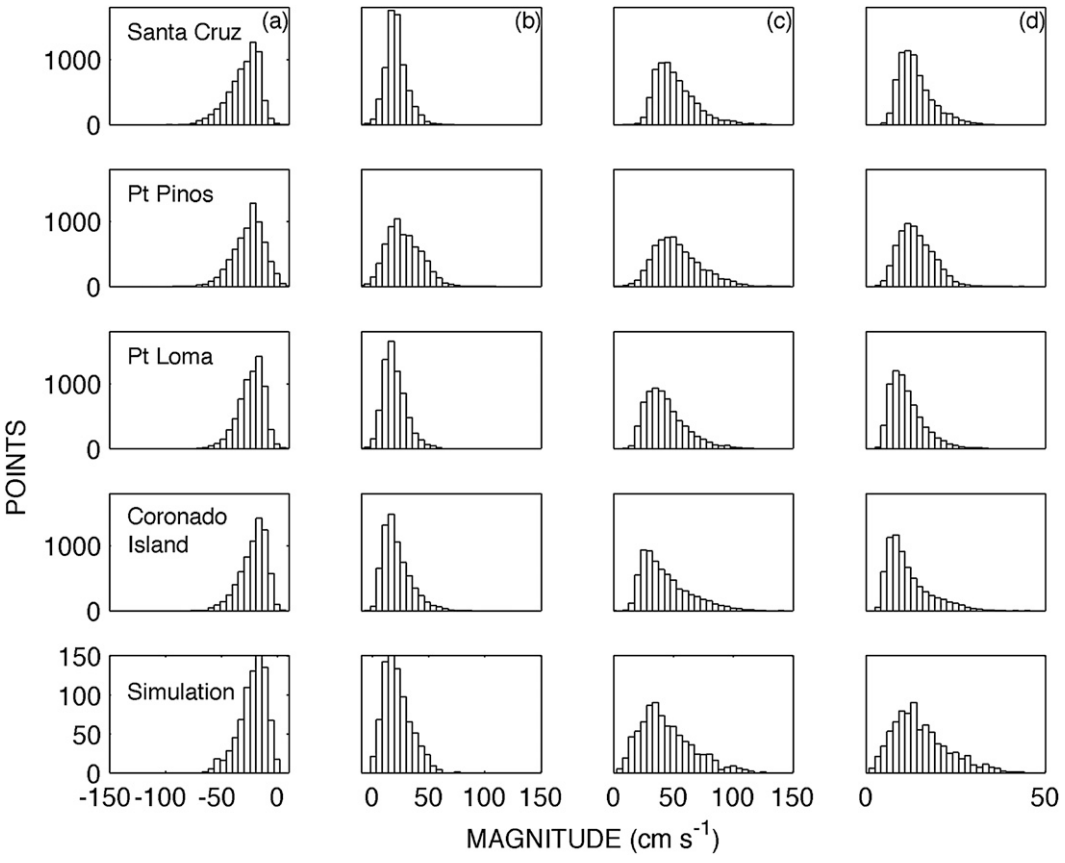

FIG. 2. Histograms of measured and simulated radial current properties for a single range arc. The radar site location (or ''simulation'') is indicated for each row. The columns show histograms of the following range arc properties: (a) minimum current on the range arc, (b) maximum current, (c) the difference between the maximum and minimum currents observed over the range arc, and (d) mean of absolute current magnitude.

discussed previously). Radial current data collected at several radar installations located along the California coast provide a statistical distribution of values for a selected set of range arc properties that are obtainable directly from the HF radar data records. Histograms of these properties for both actual radar sites and for an ensemble of simulated sea surface state scenarios are shown in Fig. 2. The simulation parameters used to generate the random sea state scenario were adjusted by trial and error to produce similar distributions in the simulated and observed range arc properties.

The purpose of evaluating these measured statistical properties is to guide the setting of simulation parameters to obtain a physically plausible ensemble of radial current profile scenarios that represent a subset of typical ocean conditions. In keeping with this goal, it is reassuring to observe that the statistical distributions of the quantities examined are similar for different radar site locations. The site at Santa Cruz covers an area within and outside Monterey Bay. The Point Pinos site has overlapping coverage but encompasses more unobstructed coastline. Both of these regions experience strong diurnal winds during spring and summer. The Coronado Island and Point Loma sites are located near San Diego, where the specific current and wind conditions are presumably very different. The Point Loma site overlaps coverage with the Coronado Island site but with a different orientation. Both sites have nonoverlapping coverage as well.

To estimate the number of points required for a given ensemble to approximate a generalized condition, we examined, for the simulation case, the variance of ensemble mean properties as a function of the number of points per ensemble. The results in Fig. 3 show, as expected, that the mean and standard deviation of the ensemble properties vary less from ensemble to ensemble as the number of points per ensemble is increased. When the number of points per ensemble is below about 200, the variance of the mean and standard deviation of the properties increase rapidly. Based on the plots in Fig. 3 and practical limitations on compute time and data storage, a value of 400 points per ensemble

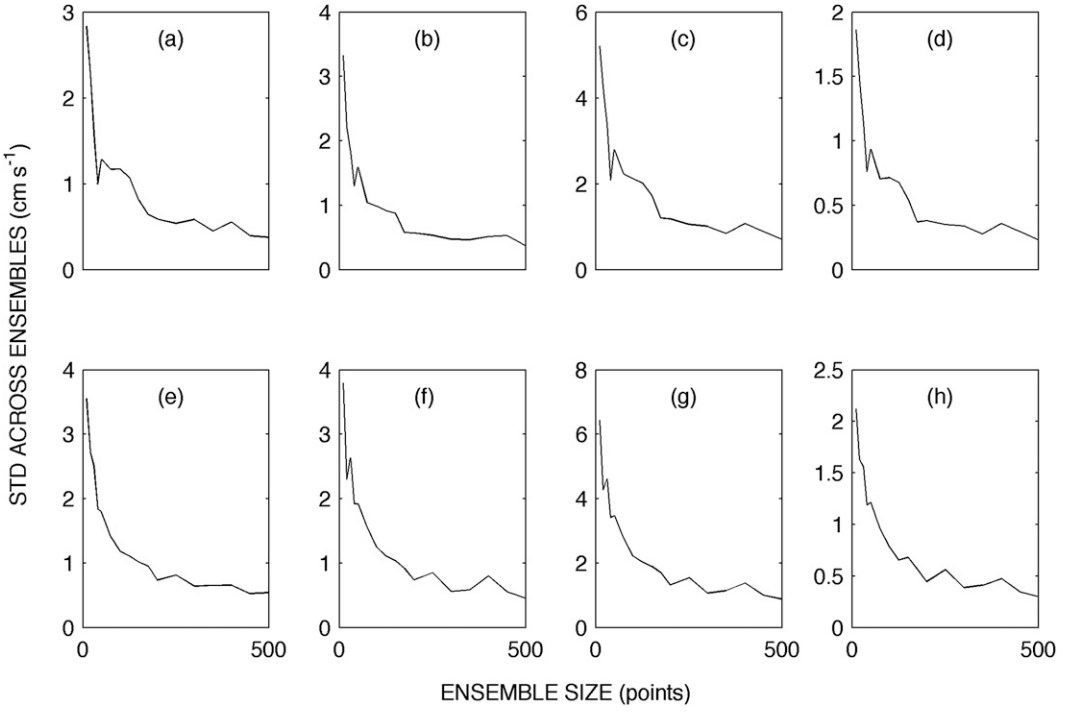

FIG. 3. Plots of the standard deviation across ensembles of the range arc radial current properties in Fig. 2 (simulation case). The standard deviations of the mean value are shown for (a) minimum current on the range arc, (b) maximum current, (c) current difference, and (d) mean of absolute current magnitude. (e)–(h) As in (a)–(d), but for standard deviations of the standard deviation of the quantities. These plots show how the width and centroid of the histograms in the previous plot vary over different ensembles, as a function of the number of points in the ensemble.

was selected as appropriate for simulations of generalized sea conditions.

To generate the simulated spectra, sea surface state conditions for each scenario were held constant over the sampling period covered by the spectra. The process was repeated to generate 400 sets of spectra files. The parameters that determine the sea conditions of a given scenario were randomly selected for each sampling period.

4. Simulation experiments

a. Ideal antenna pattern

To obtain a benchmark for radial current uncertainty, two ''best case'' scenarios are examined. The first case uses a linear current profile (a radial current magnitude that is a linear function of the radar look angle), an ideal antenna pattern, and a high SNR. This simple scenario illuminates a limiting source of error: namely, the radial current resolution of the radar observation. The radial current speed resolution Δv is dependent on the radar operating frequency and sampling time and is given by

$$\Delta v = \frac{\lambda_r}{2T} = \frac{c}{2n\Delta t f_r}, \tag{6}$$

where λ_r is the radar electromagnetic wavelength and T is the sampling time over which a single spectrum is collected; equivalently, n is the number of samples in the spectrum, Δt is the sampling interval, f_r is the radar operating frequency, and c is the speed of light. For the radar parameters used here, $n = 512$, $\Delta t = 0.50$ s, $f_r = 12.1453$ MHz, and $\Delta v = 4.82$ cm s^{-1}. From the simulation results, the rms radial error for this scenario is 1.9 cm s^{-1}, with about 80% of the errors uniformly distributed within one unit of current speed resolution Δv and the other 20% between one and two units of the resolution.

The second case examined involves generalized, random sea surface state scenarios with ideal antenna patterns and high SNR. An ensemble of 400 scenarios, with statistical properties as described in the previous section, and corresponding sets of spectra files were generated. The rms error is computed using all retrieved radial currents from a single simulated range arc from 400 hourly radials files. About 15 000 radial currents were retrieved from the 400 h of simulated spectra files.

As seen in Fig. 4, the retrieved currents are statistically similar to the simulated input currents. The standard deviations of the input and retrieved currents are

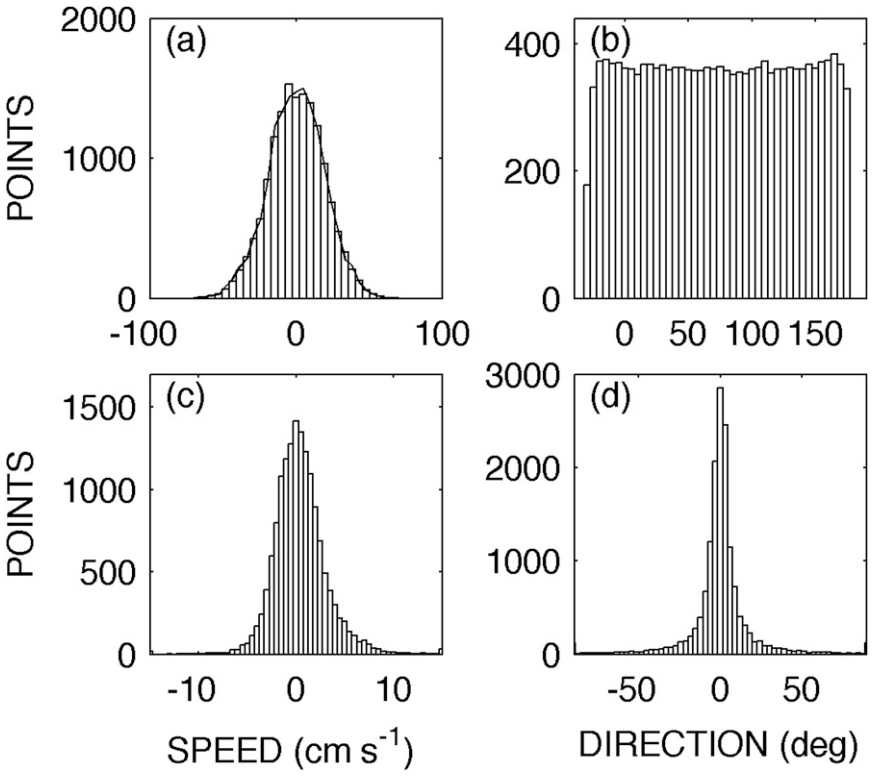

FIG. 4. Statistical analysis of hourly current estimates from simulated spectra corresponding to an ensemble of 400 different sea surface state scenarios, processed using ideal antenna patterns. The histograms show (a) the retrieved current signed magnitude, (b) the retrieved current bearings, (c) the magnitude error, and (d) the bearing error. The solid line in (a) indicates the distribution of the simulation input currents.

both 19 cm s^{-1}, and the mean of the input and retrieved currents are 0.12 and 0.55 cm s^{-1}, respectively. The histogram of retrieved directions (Fig. 4b) shows an indication of a slight increase in the number of retrieved currents for certain angular bins near the edges of the defined sea arc, −30° to 180°. Some SeaSonde users have observed increased numbers of radial retrievals near the edges of the sea arc in real data, although this is not known to be reported in the literature and the effect seen here is possibly insignificant. The averaged number of retrieved currents as a function of radar look angle is a common diagnostic used in evaluating a given radar system's performance. The simulated current magnitude errors (Fig. 4c) range from a minimum of −33 to a maximum of 42 cm s^{-1}. The skewness and kurtosis of the distribution of errors are 29 cm^3 s^{-3} and 1600 cm^4 s^{-4}, respectively. The number of simulated radials with errors in the tails of the distribution is one factor that accounts for differences between the distribution of the simulated errors and a normal distribution. For the simulated data, the rms radial current retrieval error is about 2.9 cm s^{-1} and the rms direction error of the retrievals is 23°. The mean magnitude and direction errors are 0.43 cm s^{-1} and 0.35°, respectively. The rms direction error is larger than would be expected from looking at the plot because of the flattening of the tails of the distribution. The number of radials with very large direction errors as well as the large value obtained for rms direction error are likely related to the fact that the direction associated with a given current magnitude is not necessarily single valued. Hence, very large direction errors can correspond to small-magnitude errors.

b. Distorted antenna patterns

Measured antenna patterns, consisting of the complex amplitude ratios between each of the two crossed-loop elements and the monopole as a function of direction, were obtained for several radar sites within or around the Monterey Bay region, as well as from San Diego and San Luis Obispo, California. These amplitude ratios are commonly referred to as antenna loop ratios or simply as antenna patterns. Generally, antenna pattern measurements are acquired using a small boat equipped with a GPS and a transponder or a signal generator and a transmitting antenna. The boat is piloted in an arc around the radar site, covering as large a section of

angular arc as possible, at a range of about 1 km from the radar system antennas. While the boat is transecting the arc, the receive antenna voltages and the position of the boat are continuously recorded.

The loop ratios for each of the loop antennas are recorded to a disk file used later to calibrate the radar system using the data processing software. An ideal pattern has a sinusoidal dependence on look angle for both the real and imaginary components of the loop ratios. The phase difference between the loop ratios for the two loop antennas is ideally 90°, and the phase difference between the real and imaginary components for each loop ratio is ideally either 0° or 180°. The measured patterns contain both real deviations from the ideal pattern and errors resulting from the measurement process often observed as large, high-wavenumber fluctuations. For more information on CODAR antenna pattern measurements and the effects of distortion on the current measurements, refer to Kohut and Glenn (2003). For the measured patterns used in this simulation study, no attempt was made to separate real pattern variations from measurement errors. Hence, the patterns used may contain unnaturally large, high-wavenumber fluctuations. In spite of this, the spectral distribution of the measured patterns used (see, e.g., Fig. 5) indicates that the lower-wavenumber fluctuations dominate the distortions.

The normal method for viewing the loop ratios is to convert the real and imaginary component signals to phase and amplitude. The amplitudes of the ideal patterns then depend on the absolute value of the cosine of the radar look angle, and the phases are constant, except at the antenna sensitivity nulls, where they undergo a 180° phase change. For the purpose of fitting an ideal function to a measured pattern, it is simpler to use the real and imaginary regime. A fit to the measured pattern is obtained by minimizing the function

$$f_n = \sum_{i=1}^{N} [L'_n(\theta_i) - L_n(\theta_i)]^2, \tag{7}$$

where

$$L'_n(\theta_i) = a_n + b_n \cos(\theta_i + c_n) \tag{8}$$

is an ideal fit to the measured pattern, L_n is the measured loop ratio, θ_i is the bearing direction of the pattern measurement data, N is the total number of points in the measured pattern, and $n = 1, 2$ denotes the given loop antenna. The three coefficients are the offset a, the amplitude b, and the phase c of the fit. The fitting procedure is repeated for the real and imaginary parts of both loop ratios in the measured pattern. The ideal fit to a loop pattern differs from an ideal pattern in that the offsets, amplitudes, and phases of both the real and imaginary components of each loop ratio can vary independently. For an ideal pattern, the amplitudes are all equal, the offsets are zero, and the phase relationships are fixed. An example of a measured pattern and the ideal fit is shown in Fig. 6.

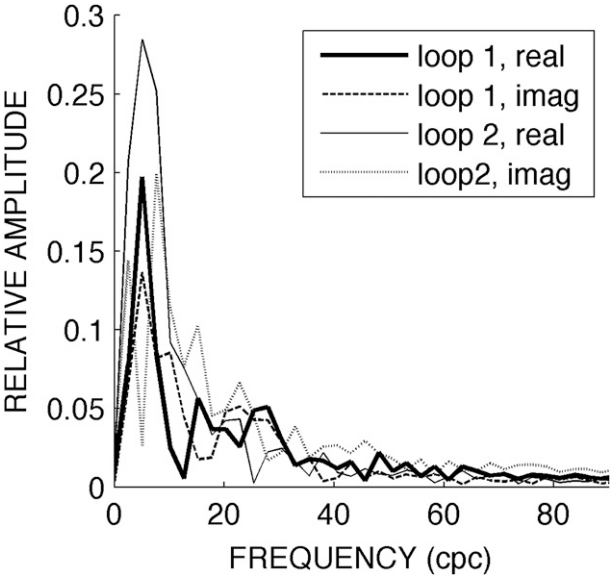

FIG. 5. Fourier analysis of deviations from the fits for the measured antenna pattern shown in Fig. 6. Deviations shown here are typical for the measured patterns used in this work. The spectral density curves plotted were scaled to be equal to the loop ratio amplitude. For example, the real component of loop 2 shows a peak spectral component with an amplitude of about 0.3 at about 7 cpc. This deviation from ideal can be seen in Fig. 6.

To increase the number of distorted patterns and the range of level of distortion in the patterns, simulated distorted patterns were generated. Simulated distorted patterns enable adjustment of the level of distortion to extend the set of measured patterns to include more extreme cases and to fill any gaps in the level of distortions in the measured pattern dataset. To generate the simulated distorted patterns, harmonic functions are first generated that approximate the amplitude as a function of angle for each of the loop ratios, given by

$$\overline{L''_1}(\theta) = A_1 \cos(\theta + \delta\phi_{1\alpha}) - iB_1 \cos(\theta + \delta\phi_{1\beta}) \quad \text{and} \tag{9}$$

$$\overline{L''_2}(\theta) = A_2 \sin(\theta + \delta\phi_{2\alpha}) - iB_2 \sin(\theta + \delta\phi_{2\beta}) \tag{10}$$

with normally distributed random deviations of the expected phase and amplitude coefficients. The mean value of the amplitudes A and B was set to 0.5, and the standard deviation was 0.33. The mean phases were set equal to the ideal phase values with a standard deviation

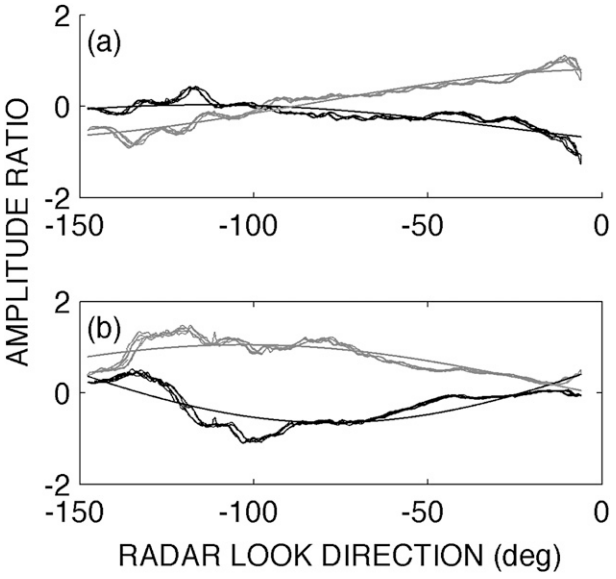

FIG. 6. An example of fits (smooth curves) to the real (black line) and imaginary (gray line) parts of measured antenna patterns for (a) loop 1 and (b) loop 2. The measured antenna pattern shown was collected at the Santa Cruz radar site, Monterey Bay, on 16 Mar 2007. Patterns were measured using a boat carrying a transponder along an arc centered on the radar site. Multiple lines appear in the plots because five passes of the boat were done to obtain more accurate estimates of the loop ratios through averaging. This example is a mildly distorted case ($\langle\Gamma\rangle = 0.35$).

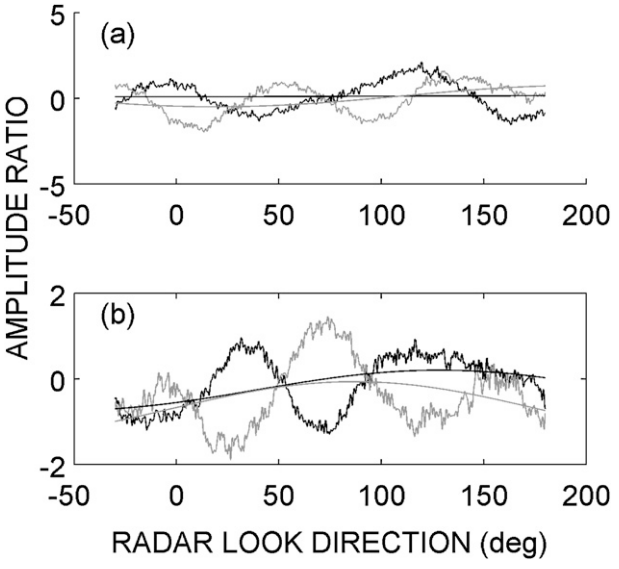

FIG. 7. Plots of the real and imaginary components of the loop ratios for a simulated distorted antenna pattern: (a) loop 1 and (b) loop 2. This example is an extremely distorted case ($\langle\Gamma\rangle = 2.2$). Examples of measured patterns from field sites showing this level of distortion were not readily available. The smooth curves are the ideal fits. The real components are shown in black line, and the imaginary components are shown in gray.

of 28°. These values were derived empirically from observations of measured patterns. Distortions are then added to the basic amplitude functions using

$$L_n''(\theta) = \overline{L_n''} + \sum_{j=1}^{N} C_j \cos(j\theta + \phi_j), \tag{11}$$

where $N = 350$ sets the upper limit on the frequency of the added distortions and the harmonic coefficients C_j follow an empirically derived functional form. Both the functional form of C_j and the value of N were obtained through examinations of the Fourier transform of distortions in measured loop ratios. In this case, frequency corresponds to cycles per circumvolution (cpc) of the radar look direction. A typical example of the Fourier transform of distortions relative to an ideal fit is shown in Fig. 5 for the measured antenna pattern shown in Fig. 6. A plot of a simulated distorted pattern, along with the ideal fit, is shown as an example in Fig. 7.

c. Parameterization of antenna pattern distortions

There are many possible parameters that may be used to describe the differences between ideal fits and measured patterns; some of these include magnitude differences between the measurements and the fits, phase differences between the fits and the ideal pattern, differences in amplitudes and offsets of fits from expected values, and characteristics of the Fourier spectrum of the differences between measured patterns and fits. These parameters were each investigated for skill in predicting errors in the simulated radial current measurements. Only one parameter was found to exhibit skill in predicting simulated radial current errors, and that was the absolute difference in magnitude between the measured pattern and the fits. This result is somewhat surprising, as one might expect that deviations in the phase relationship between the loop ratios would be important. The results suggest that these phase relationships, as exhibited by the patterns examined here, are not important as long as they are well known. It should be noted, however, that none of the antenna patterns examined had such a level of distortion that the loops could be approximated as parallel. In that case, the inversion method would be expected to break down.

The skill of the distortion magnitude parameter was found to be improved when scaled by a loop ratio magnitude, defined for each of the loops as the mean magnitude of the fit over the range of radar look angles in the measured pattern. The scaled distortion magnitude parameter as a function of azimuth is given by

$$\delta L_n(\theta) = \frac{|L_n' - L_n|}{\langle |L_n'| \rangle}, \tag{12}$$

where L_n represents the measured loop ratios for the two loops, L'_n represents the previously described fits to the measured patterns, and the angle brackets indicate ensemble average over radar look angles. The scaled distortion magnitude parameters for each of the two loops in the antenna system are then averaged together to arrive at a single antenna distortion parameter given, as a function of radar look angle, by

$$\Gamma(\theta) = \frac{1}{2}[\delta L_1(\theta) + \delta L_2(\theta)]. \quad (13)$$

The mean of this distortion parameter over all radar look angles $\langle \Gamma(\theta) \rangle$ provides a single scalar parameter describing the pattern distortion.

d. Simulating and processing data with distorted antenna patterns

Ensembles of simulated spectra files corresponding to 400 random sea surface state scenarios were generated for each of 40 different antenna patterns. The antenna patterns included 19 measured patterns from sites located on the California coast near Monterey Bay, San Luis Obispo, and San Diego, as well as 20 simulated distorted patterns and the ideal pattern. In each antenna pattern case, the antenna response characteristics were used in computing the simulated spectra received by the radar as well as in the data processing. The simulated spectra files were processed using CODAR's radial current retrieval algorithm and typical radar operating parameter settings. Some of the pertinent data processing parameter settings are given in Table 1. Descriptions of the data processing parameters are provided in CODAR's documentation, which is available from the company's Web site (available online at http://www.codaros.com).

When processing these simulated radar spectra, antenna pattern measurement data are read by the data processing software from a text file with a specific format. In practice, the angular resolution of the pattern measurement data contained within this file is left up to the user, but typically a coarser resolution is selected compared to the resolution of the antenna pattern measurement. This is done because it is generally believed that the measured patterns contain high-wavenumber noise and that the actual antenna pattern is better represented by a smoothed measured pattern. The optimal degree of smoothing has not been definitively established. For the measured patterns used here, the angular resolution of the raw data is typically between 0.1° and 0.3°. The simulated-distorted patterns were generated with a resolution of 0.1°. In generating the simulated radar spectra, the full resolution of the antenna patterns was retained. For the retrieval data processing, the patterns were smoothed by averaging to a resolution of 1°. Apart from smoothing, the antenna pattern used to retrieve the radial currents was the same as the pattern used for generating the simulated signals received by the antennas.

TABLE 1. Data processing parameter settings.

Parameter	Setting used
MUSIC parameter settings	40, 20, 2
Averaging time	1 h
Estimated max current	150 cm s^{-1}
No. of points for running average	1
No. of frequency points	512
Factor down peak	15
Second-order processing	No
Factor down peak nulls	7.5
Noise factor	4.0
Coverage time	74 min
Output interval	60 min
Transmit frequency	12.1453 MHz
Frequency increment	0.003 906 25 Hz
Angular resolution	5°
Averaging period	15 min
Output period	10 min
Thresholding	After 8 input files
Threshold value	12.0
Smoothing	No

5. Results

a. Skill of antenna distortion parameter

For each of the 40 different antenna pattern cases, the rms radial current error is computed for all retrievals from a single range arc from 400 simulated hourly radial files. The number of simulated radial current measurements is about 13 000 for each antenna pattern case. Figure 8 shows the cumulative error distribution functions for the approximately 13 000 simulated radials for each of three selected cases, a pattern with no distortions; a measured pattern from the Naval Postgraduate School radar site, Monterey Bay, with a distortion pattern value of 0.49 (near the median of the antenna patterns investigated); and a simulated distorted pattern with a value of 1.5 (near the maximum of the patterns investigated). For the three cases, the magnitude errors below 5 cm s^{-1} account for about 95%, 78%, and 75% for the undistorted, medium, and badly distorted cases, respectively. Similar percentages of errors accounted for direction errors of about 25°. Figure 9 shows the scatterplot of rms error as a function of antenna pattern distortion. With both measured and simulated-distorted antenna pattern results combined, a linear regression model relating the antenna distortion parameter to the rms error predicts about 88% of the variance in the rms

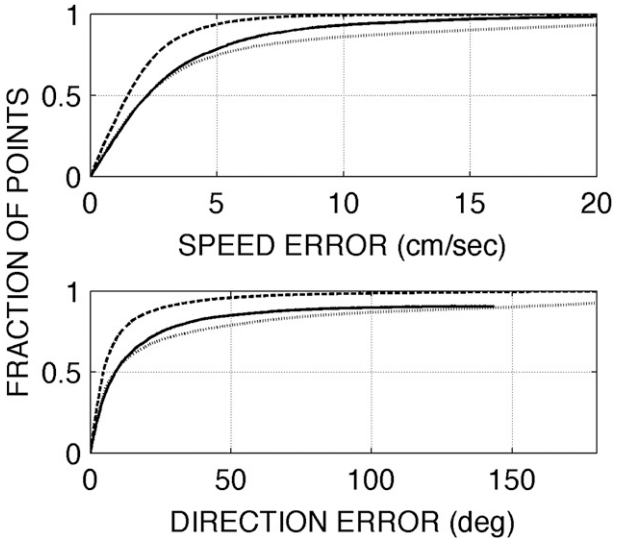

FIG. 8. Integrated error in radial current retrievals from simulated data, expressed as the fraction of data points below the abscissa value as a function of the error magnitude for (top) current speed errors and (bottom) current bearing errors. The three lines correspond to different antenna pattern scenarios: ideal patterns (dashed line), measured pattern with antenna distortion parameter = 0.49 (solid line), and simulated pattern with antenna distortion parameter = 1.55 (dotted line).

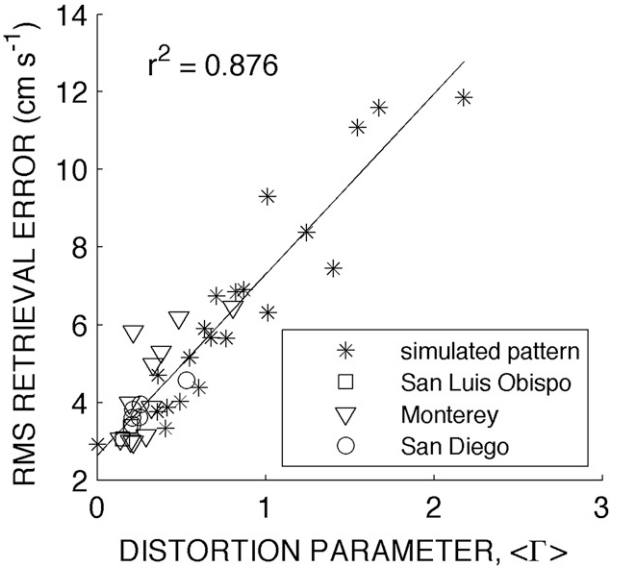

FIG. 9. Scatterplot of the simulated rms radial current error vs the antenna pattern distortion parameter. The open symbols correspond to results from using measured antenna patterns, with the region of the radar site indicated by the legend. The asterisks correspond to results with simulated-distorted patterns. The correlation coefficient given is for measured and simulated-distorted pattern results combined. Individually, the correlation coefficient for the measured antenna pattern results is 0.751; for the simulated-distorted pattern results, the correlation is 0.939.

error for the 40 different antenna pattern cases examined. Of the 19 measured patterns we examined, the mean value of the distortion parameter was 0.29 and the standard deviation of values was 0.16. The minimum and maximum values were 0.14 and 0.81, respectively.

Error as function of radar look angle was also examined. However, the results were inconclusive. Figure 10 shows a typical example of the results obtained. As seen in the figure, no clear relationship between angular dependence of rms errors or number of retrievals and the directional features of the antenna pattern distortion function is indicated. This is somewhat surprising given the strong correlation between overall rms radial errors and the mean distortion function values. For each of the antenna patterns examined, the lack of obvious correlations is similar to those shown in the figure.

b. Subperiod standard deviation (temporal quality)

The dependence of the subperiod radial standard deviation, referred to by CODAR as the temporal quality (described in section 3a) on the antenna distortion parameter is shown, for both simulated and real data, in Fig. 11. For the simulated data, a clear dependence is indicated with a correlation coefficient of over 0.90. This is similar to the correlation observed between the rms error of the retrievals and the antenna distortion parameter.

The real data, obtained from several field sites in the Monterey Bay region, are approximately month-long time series. Plotted are the mean values of the subperiod standard deviation over all times and angular resolution cells within the third range bin. Range bin 3 was selected for this analysis as a compromise between maximizing SNR and preserving a somewhat similar relationship between the size of a range/azimuth cell in the real data and in the simulated data. The field site data all demonstrate higher mean subperiod standard deviation than those obtained from the simulation results, and no correlation is apparent between the mean subperiod standard deviation and the antenna distortion parameter. These results are surprising and not completely understood. The higher than expected mean subperiod standard deviation values and lack of correlation may be due to effects of lower SNR of specific measurements (possibly because of interference from higher-order scatter, ship echoes, or other sources), real temporal variability in the ocean currents during the sampling period of the hourly measurements, or other sources of error not accounted for in the simulation.

6. Conclusions

The relationship between errors in simulated CODAR SeaSonde HF radar–based ocean current measurements

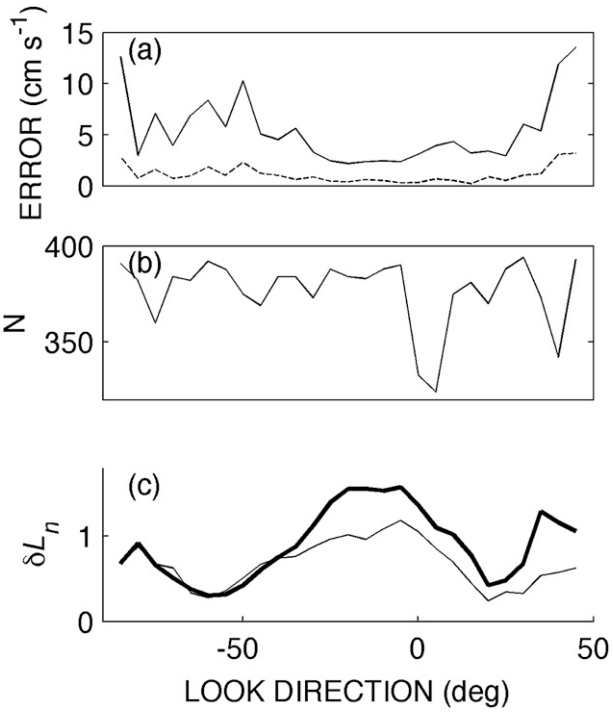

FIG. 10. Directional characteristics of (a) mean (dashed line) and standard deviation (solid line) of errors in simulated radial retrievals; (b) number of retrievals per angular resolution cell; and (c) normalized loop ratio distortion for the two loops, loop 1 (thick line) and loop 2 (thin line), for the measured pattern with the largest distortion parameter, the Monterey Bay site located near the Naval Postgraduate School.

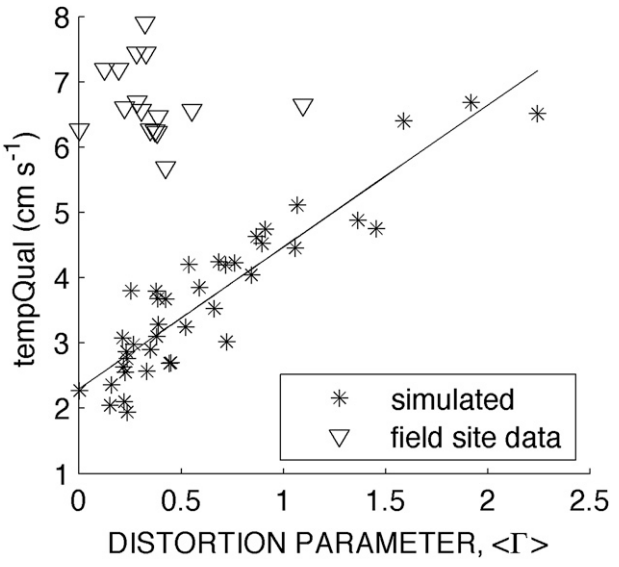

FIG. 11. Mean subperiod standard deviation as a function of antenna pattern distortion for both simulation results and field site data. The field site data were obtained from approximately one-month time series containing a similar number of radial retrievals as with the simulation results. The correlation coefficient for the simulated data results is $r = 0.918$.

and the associated antenna patterns used in data processing with those systems has been examined. To avoid limiting the applicability of the results to specific ocean current and wind wave scenarios, analyses are based on ensembles of simulated random current and wind scenarios that produce radial current profiles with the desired characteristics. These characteristics include large changes in the variation of current speed with azimuth and situations with single, double, and triple valued solutions for direction for a given current speed. Maximum current speeds were limited to about 75 cm s^{-1}. Parameters used to generate the scenarios were set so that selected statistical properties of the radial current profiles were similar to those obtained from field site data from sites along the California coast. The conclusions presented here are based on analyses that include 40 different antenna patterns, both simulated-distorted patterns and measured patterns from field sites.

For simulated radar backscatter generated under minimally challenging conditions (i.e., a linear current profile, high SNR, and ideal antenna patterns), radials produced by processing the simulated data with standard CODAR SeaSonde software, with a Doppler current resolution of 4.8 cm s^{-1} and a directional resolution of 5°, were found to have an error standard deviation of 1.9 cm s^{-1}.

For simulated data corresponding to a large ensemble of random wind wave and current scenarios and ideal antenna patterns, the retrieved radials obtained using the same data processing method have an rms error of 2.9 cm s^{-1}. This level of error represents a minimum bound on the error of a SeaSonde ocean radar system, given a typical set of operating parameters and a generalized ensemble of ocean conditions statistically similar to those observed at radar sites along the California coast.

The effect of distortions in the antenna sensitivity patterns on the simulated radial current errors is examined for 40 different antenna pattern cases. The results demonstrate that the level of pattern distortion can be parameterized by comparing the real and imaginary components of the antenna sensitivity patterns with ideal fits. The antenna distortion parameter is found to be highly correlated ($r = 0.94$) with the rms error of the corresponding simulated radial current retrievals.

The mean magnitude of a data quality indicator produced by the CODAR data processing software was also compared with the antenna distortion parameter over the range of antenna pattern distortion cases. This data quality indicator is the standard deviation of intermediate values of the radial current estimates used by

the processing software to compute the final current estimates. For simulated data, the indicator is found to be highly correlated with the antenna distortion parameter ($r = 0.92$). Because both the antenna distortion parameter and data quality indicator can be measured directly from field site data, it is possible to compare field site results with the simulation results. For field site data, no correlation between the mean data quality indicator and the antenna distortion parameter is indicated. This result is surprising and not completely understood. The results indicate that other sources of error or variability in the radial current estimates dominate over antenna pattern distortion effects in the field site data.

The results presented here indicate that antenna pattern distortions can be characterized using a single parameter that is, in the absence of other sources of error, well correlated with the errors in simulated radial current retrievals. This parameter can enable users of CODAR SeaSonde systems to evaluate the likely contribution of their observed antenna pattern distortions to errors in the system's radial current measurements. These simulation results show that antenna pattern distortions account for an increase in rms error, even when data are processed using the appropriate distorted patterns, from about 2.9 cm s^{-1} for patterns with no distortions to about 12 cm s^{-1} for the most distorted of the patterns examined.

Acknowledgments. The authors thank the National Science Foundation for supporting this project under Grants 0526978 and 0526614. The authors also thank Dr. Annalisa Griffa for providing consultation on this project and its application to data assimilation; both Annalisa Griffa and Dr. GianPietro Gasparini for hosting Kenneth Laws at the Consiglio Nazionale delle Ricerche (CNR), Istituto di Scienze Marine (ISMAR), La Spezia during the scope of this project; Brian Emery and Brian Zelenke for sharing SCCOOS antenna pattern data and to Dan Atwater for sharing CeNCOOS antenna pattern data; and Don Barrick for providing an early release of CODAR software for this study.

REFERENCES

Barrick, D. E., and J. B. Snider, 1977: The statistics of HF sea-echo Doppler spectra. *IEEE Trans. Antennas Propag.,* **2,** 19–28.

——, and B. J. Lipa, 1997: Evolution of bearing determination in HF current mapping radars. *Oceanography,* **10,** 72–75.

Breivik, O., and O. Saetra, 2001: Real time assimilation of HF radar currents into a coastal ocean model. *J. Mar. Syst.,* **28,** 161–182.

De Paolo, T., and E. Terrill, 2007: Skill assessment of resolving ocean surface current structure using compact-antenna-style HF radar and the MUSIC direction-finding algorithm. *J. Atmos. Oceanic Technol.,* **24,** 1277–1300.

Emery, B. M., L. Washburn, and J. A. Harlan, 2004: Evaluating radial current measurements from CODAR high-frequency radars with moored current meters. *J. Atmos. Oceanic Technol.,* **21,** 1259–1271.

Kohut, J. T., and S. M. Glenn, 2003: Improving HF radar surface current measurements with measured antenna beam patterns. *J. Atmos. Oceanic Technol.,* **20,** 1303–1316.

Laws, K. E., D. M. Fernandez, and J. D. Paduan, 2000: Simulation-based evaluations of HF radar ocean current algorithms. *IEEE J. Oceanic Eng.,* **25,** 481–491.

Lipa, B. J., B. Nyden, D. S. Ullman, and E. Terrill, 2006: SeaSonde radial velocities: Derivation and internal consistency. *IEEE J. Oceanic Eng.,* **31,** 850–861.

Longuet-Higgins, M. S., D. E. Cartwright, and N. D. Smith, 1963: Observations of the directional spectrum of sea waves using the motions of a floating buoy. *Ocean Wave Spectra,* Prentice-Hall, 111–136.

Milligan, T. A., 2005: *Modern Antenna Design*. Wiley Interscience, 614 pp.

Paduan, J. D., and I. Shulman, 2004: HF radar data assimilation in the Monterey Bay area. *J. Geophys. Res.,* **109,** C07S09, doi:10.1029/2003JC001949.

——, P. M. Kosro, and S. M. Glenn, 2004: A national coastal ocean surface current mapping system for the United States. *Mar. Tech. Soc. J.,* **38,** 102–108.

——, K. C. Kim, M. S. Cook, and F. P. Chavez, 2006: Calibration and validation of direction-finding high frequency radar ocean surface current observations. *IEEE J. Oceanic Eng.,* **31,** 862–875.

Pierson, W. J., and L. Moskowitz, 1964: Proposed spectral form for fully developed wind seas based on similarity theory of S. A. Kitaigorodskii. *J. Geophys. Res.,* **69,** 5181–5190.

Schmidt, R. O., 1982: A signal subspace approach to multiple emitter location and spectral estimation. Ph.D. dissertation, Stanford University, 201 pp.

——, 1986: Multiple emitter location and signal parameter estimation. *IEEE Trans. Antennas Propag.,* **34,** 276–280.

Sheres, D., K. E. Kenyon, R. L. Bernstein, and R. C. Beardsley, 1985: Large horizontal surface velocity shears in the ocean obtained from images of refracting swell and in situ moored current data. *J. Geophys. Res.,* **90** (C3), 4943–4950.

Shulman, I., and J. D. Paduan, 2008: Assimilation of HF radar-derived radials and total currents in the Monterey Bay area. *Deep-Sea Res.,* **56** (3–5), 149–160.

Toh, K.-Y. D., 2005: Evaluation of surface current mapping performance by SeaSonde high frequency radar through simulations. M.S. thesis, Naval Postgraduate School, 123 pp.

Wu, J., 1975: Wind induced drift currents. *J. Fluid Mech.,* **68,** 49–70.